

EXPERIMENTAL CHARACTERIZATION OF INTERCHANNEL MIXING THROUGH A NARROW GAP

Simo A. Mäkiharju and Steven L. Ceccio

Department of Naval Architecture and Marine Engineering
University of Michigan
Ann Arbor, MI 48109, USA
smakihar@umich.edu

John R. Buchanan, Jr., Alexander G. Mychkovsky, Kevin J. Hogan, and Kirk T. Lowe

Bettis Atomic Power Laboratory
Bechtel Marine Propulsion Corporation
West Mifflin, PA 15122, USA

ABSTRACT

The mass transfer through gaps connecting two adjacent channels was investigated as a function of gap geometry and flow conditions. An experiment with a simplified geometry was conducted to aid in the physical understanding and to provide data for validation of numerical computations. The flow loop consisted of two channels with two interchangeable test sections. The inlet Reynolds number in each channel could be independently varied from 4×10^4 up to 1×10^5 . Measurements were performed for seven channel flow rate combinations and eleven gap heights for both test sections. The mass transfer through the gap was calculated from mass flow rate and tracer concentration measurements taken at channel inlets and outlets. Planar and tomographic particle imaging velocimetry, as well as imaging of fluorescent tracer dye, were utilized for select conditions to examine the dynamics of the mixing. Accompanying computations were performed and the results compared favorably with experimental data. For the cases of nearly balanced flow, large coherent structures forming in the gap were observed and exhibited a normalized frequency in agreement with that reported by previous investigators. Over the tested range, the mixing rate as a function of gap height was nominally independent of channel Reynolds number. For significantly unbalanced flow the measured mass transfer approached the one-way mass transfer limit, whereas for larger gaps and closer flow balance the mixing due to coherent structures became significant.

KEYWORDS

Interchannel mixing, leakage flow, coherent structures, code validation data, integral mixing, CFD validation

1. INTRODUCTION

Mixing through narrow gaps connecting adjacent primary flow paths is an important mass transfer process for many thermo-hydraulic applications, such as flows through nuclear reactor rod bundles and heat exchangers. In addition to turbulent mixing and mixing due to any pressure gradient across the gap, the flow can develop large-scale periodic flow structures. These coherent structures can substantially affect the rate of mixing between the primary flow paths. Several researchers have studied the basic flow processes of the flow between parallel flow channels connected by gaps [1-8], and a review article by Meyer [9] offers a comprehensive review of the past work on interchannel mixing. These researchers have gleaned significant insights into the underlying flow processes, including the formation of large-scale coherent structures in the narrow gaps between the channels. Interchannel mixing has been numerically investigated by numerous investigators, including Chang and Tavoularis [10, 11], Home *et al.* [12], Derksen [13], and Home and Lightstone [14]. Merzari *et al.* [15] also uses proper orthogonal decomposition to better understand the underlying dynamics of the oscillations observed in the

interchannel flow. However, few studies have produced experimental data sets that are immediately suitable for the validation of high-fidelity Computational Fluid Dynamics (CFD) models. In some reported experimental data sets, the flow inlet boundary conditions are not well characterized, the as-built dimensions of the test section are not available, or uncertainties of the instruments used are not quantified. Since the resulting flows are sensitive to small changes in boundary conditions (see Ko *et al.* [16] for example of the sensitivity of similar flows), these data are not ideally suited for rigorous CFD code Verification and Validation (V&V). Derksen [13] performed computations and compared his results with experimental data, but also noted the lack of expected symmetry in the experimental data, again suggesting that there was an underlying issue with the flow geometry, the inlet conditions, the outlet flow conditions, or some combination of effects.

This study examines the single-phase mixing through narrow rectangular gaps connecting two channels with emphasis placed on defining the geometric as-built and measurement uncertainties, quantifying the inflow conditions, and closely coordinating each stage of the experiment with an accompanying CFD V&V effort in order to produce high-fidelity V&V data sets. The goal of the experiment was to expand the parameter space explored by Meyer and Rehme [1] to determine at what gap height the mixing behavior transitions from small to large, the influence of gap width, and the appropriate means to model the behavior *via* CFD. The as-built measurements were recorded by qualified machinists, and the inlet flow conditions extensively surveyed via Laser Doppler Velocimetry (LDV) in order to verify that the flow was well-conditioned as it approached the test section gap. The bulk mass transfer through the various gap openings was determined from the mass flow rate and fluorescein tracer dye concentration measurements at the channel inlets and outlets. These measurements were performed for seven channel flow rate combinations and eleven gap heights for both test sections. Planar and tomographic Particle Image Velocimetry (PIV) and synchronized two-view high-speed video of the fluorescent tracer dye were employed at select conditions to further examine the dynamics of the mixing phenomena. CFD was performed in parallel with the experiments to aid in the interpretation of the experimental results.

The basic experimental setup, inflow conditions and numerical model are described in Section 2. Selected time-averaged results for integral mixing of both balanced and unbalanced inlet mass flow rates are presented in Section 3. Some additional detail of the observed coherent structures based on dye visualization, PIV data and CFD results are provided in Section 4, and the results are summarized in Section 5.

2. EXPERIMENTAL AND NUMERICAL SETUP

To enable laser velocimetry, dye visualization, and PIV measurements, machined and polished to optical grade acrylic and polycarbonate blocks attached to an aluminum frame were used to form the channel and gap geometries of the test sections. Figure 1 shows the test section's key dimensions. For both test sections the two square channels had a $(127 \text{ mm})^2$ cross-section.

- For Test Section (a) [TS(a)]: the gap width, W , was 50.8 mm and length, L , 914.4 mm
- For Test Section (b) [TS(b)]: the gap width, W , was 228.6 mm and length, L , 1219.2 mm

For both test sections, the gap height, H , could be varied between 0 and 50 mm.

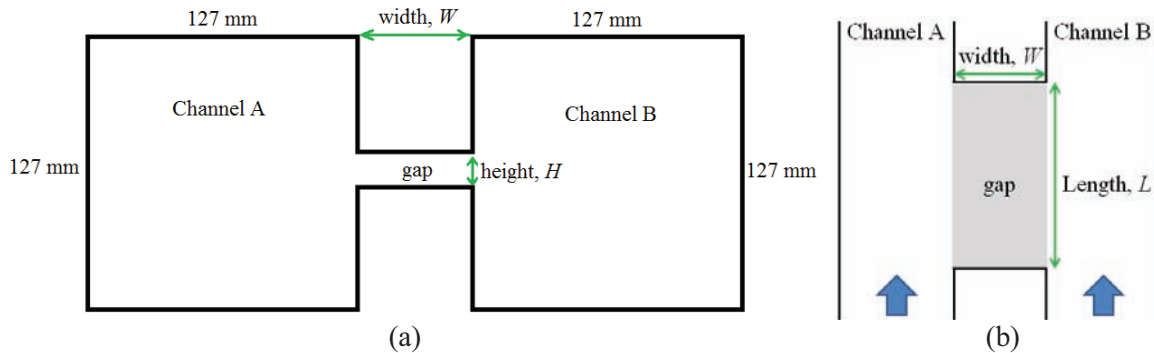


Figure 1. The geometry (not drawn to scale) of the test sections on center plane a) normal and b) parallel to the primary flow direction. Both channels had a hydraulic diameter, D_h , of 127 mm.

To measure the integral mixing, the mass flow rates at the channel inlets were measured with turbine flow meters (Omega Engineering SYS/FTB-109/FLSC-18B) with manufacturer specified accuracy $\pm 0.5\%$ of reading, and at the outlets by turbine flow meters (Omega Engineering FTB740/FTB700-T) with manufacturer specified accuracy $\pm 1\%$ of full scale (± 6 gpm). With the gap closed and no mixing, as well as when diverting the outflow to drain and monitoring source reservoir level, the flow meters were found to agree within their stated uncertainties. The absolute pressure in the test section was recorded by 0-30 psia transducer (Omega Engineering PX219-030A10V) with manufacturer specified accuracy of $\pm 0.25\%$ of full scale, and the pressure differential across the channel was recorded by 0-6 inH₂O transducer (Omega Engineering PX760-06WCDI) with manufacturer specified accuracy of $\pm 0.17\%$ of full scale, and manometers with estimated accuracy of ± 0.03 inH₂O. The water temperature was measured continuously by four 4-wire 100 ohm platinum RTD sensors (Omega Engineering P-M-A-1/4-6-0-P-3) with manufacturer specified accuracy $\pm (0.15 + 0.002|T|)^\circ\text{C}$. Fluorescein dye traced was injected upstream of channel B pump, and the tracer concentration was measured immediately upstream of the gap in both channels A and B, and in both channels far enough downstream of the gap that sampling from pipe's centerline or wall produced the same result. Fluorescein sodium salt (F6377, Sigma-Aldrich) concentration was measured by a single fluorometer (Turner Designs Cyclops 7 PN 2100-000/2108-000) with uncertainty based on calibration defined as $\pm (0.5\% \text{ or reading} + 1 \text{ ppb})$. Samples for the fluorometer were automatically drawn by a valve manifold with a clean water flush performed between each sampling location change.

2.1 Measured Inflow Conditions

The incoming flow speed in each channel could be independently varied, enabling the study of the effect of velocity difference for interchannel mixing. Nominally the Reynolds number based on the channel's hydraulic diameter in both incoming channels was varied from $Re_{Dh} = 4 \times 10^4$, 6×10^4 , 8×10^4 , to 1×10^5 . For nominally 20 °C water, these correspond to average inlet flow speeds of 0.315, 0.472, 0.630 and 0.787 m/s, respectively.

At $Re_{Dh} = 10^5$ to have a fully developed channel flow upstream of the gap would have require greater than 36 channel hydraulic diameters of run-up length (*approximately* 4.6 m) [17], and hence it was decided to forgo having a fully developed inflow. The inflow boundary layer was tripped downstream of a 6-to-1 asymmetric contraction and the flow conditions upstream of the gap were thoroughly surveyed by performing LDV scans of the axial velocity spanning the entire channel cross-section of the channel, and 1D boundary layer (BL) scans. For the inflow LDV data, the gap was closed. The LDV data was post-processed in Matlab, where velocity subranging was also employed to remove any erroneous near zero velocity bursts from the data. Fig. 2 shows the boundary layer profiles and Fig. 3 shows a sample 2-D slice of the inflow and note that the inlet flow was nearly symmetric with no strong secondary flows in the corners.

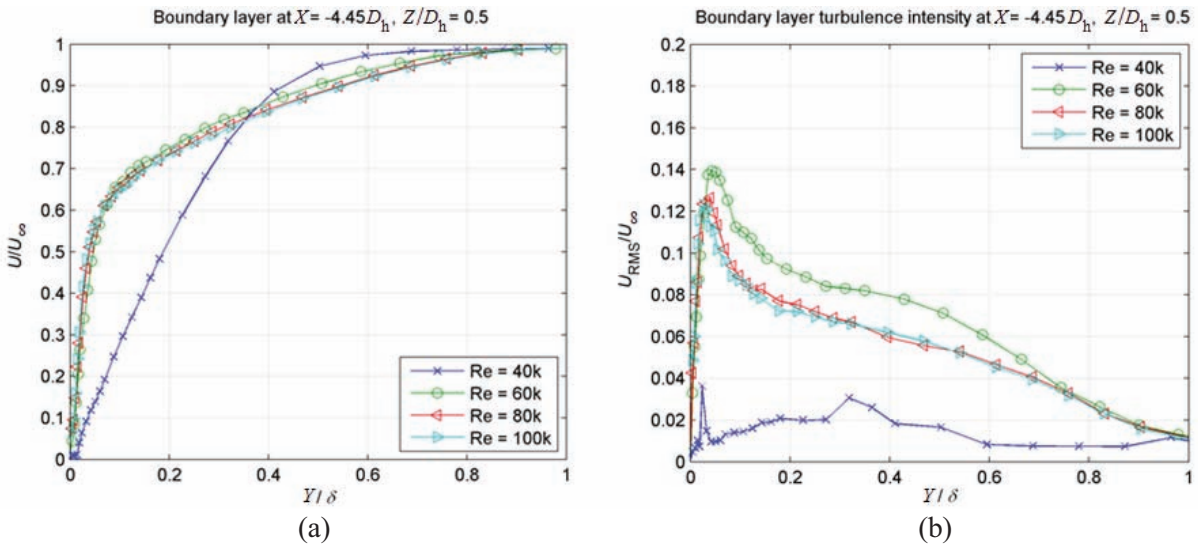


Figure 2. The boundary layer profiles of (a) the average and (b) RMSD streamwise velocity at various Reynolds numbers at $x = -4.45D_h$ in TS(a). Location $x = 0$ at the beginning of the gap.

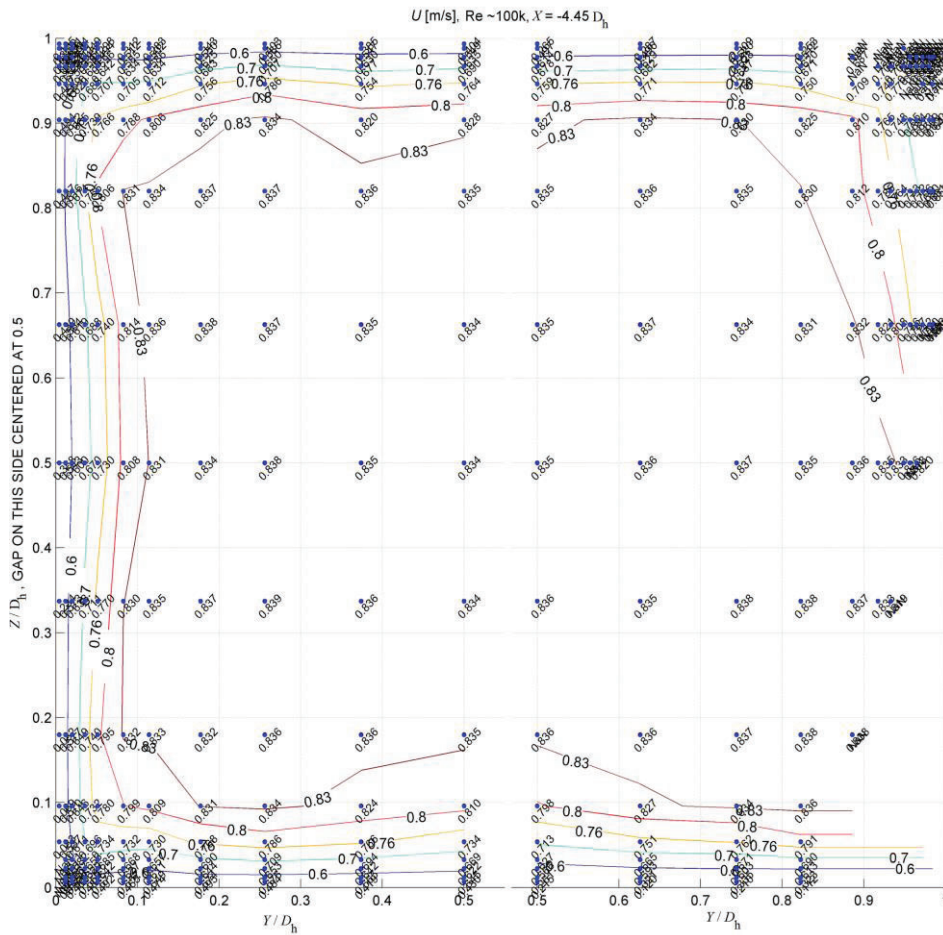


Figure 3. Contours of streamwise velocity at Reynolds numbers 10^5 at $X = -4.45D_h$ in TS(a). The channel was scanned in two sections overlapping at $Y/D_h = 0.5$, and the lower right corner was in the shadow of the channel's frame. Gap is centered at $Z/D_h = 0.5$ at $y/D_h = 1$.

As the wall shear stress is an important physical quantity and also used to scale the profiles of turbulent boundary layers, but was not directly measured in the current experiments, the Clauser plot method [19] was employed to estimate local shear stress. However, while according to Tropea [20] this method is capable of yielding the value to within $\pm 5\%$, for the estimation of uncertainty in the present study, it was taken to have uncertainty of $\pm 20\%$. Table 1 lists the key boundary layer (BL) details for the flow conditions of interest. The “free stream speed” outside the BL in the core of the flow is U_∞ , and BL thickness is taken at $U = 0.99U_\infty$. The displacement δ^* and momentum thicknesses θ are from integrals taken from the wall, where, by definition, the velocity was set to zero, up to δ , and we get the shape factor, $H_s = \delta^*/\theta$. For the Reynolds number 40,000 case, the BL was nearly laminar at the streamwise measurement location. Hence, for this case the shear stress was evaluated from the linear slope near wall, and not from a Clauser plot. Additionally, the channel A and B, as well as TS(a) and TS(b), BL data were found to be in agreement.

Table 1. Details of the boundary layer. τ_w is the shear stress, $u_\tau = \sqrt{\tau_w/\rho}$ is the frictional velocity and, $l^+ = \nu/\sqrt{\tau_w/\rho}$ the viscous length. The latter two were calculated assuming $T_w = 20^\circ\text{C}$ and hence $\rho = 998.3\text{ kg/m}^3$ and $\nu = 1.004 \times 10^{-6}\text{ m}^2/\text{s}$.

Nominal Re_{Dh}	U_∞ [m/s]	$\delta \times 10^3$ [m]	$\delta^* \times 10^3$ [m]	$\theta \times 10^3$ [m]	H_s	Estimated C_f	τ_w [N/m ²]	u_τ [m/s]	$l^+ \times 10^6$ [m]
100,000	0.84	13.8	2.2	1.5	1.5	0.0039	1.4	0.037	27
80,000	0.67	13.8	2.2	1.5	1.5	0.0042	0.95	0.031	33
60,000	0.50	12.7	1.9	1.3	1.5	0.0046	0.59	0.024	41
40,000	0.34	10.8	2.4	1.0	2.4	0.0015*	0.084	0.009	109

2.2 The Computational Model

The geometry of the University of Michigan test section was provided *via* CAD files and manipulation of the nominal geometry was performed in ANSYS Workbench (v. 14.5, Canonsburg, PA) using the Design Modeler module. In particular, the structural components needed to be made water tight and inverted to create the water volume and wetted surfaces. This model included the asymmetric contractions located upstream of the flow conditioning elements. With the inlet boundary conditions measured for both test sections, the decision was made to trim the upstream contractions and flow conditioning out of the model. The inlet of the model corresponded to the axial location where the inlet boundary conditions were measured, $x/D_h = -4.45$ upstream of the start of the gap. The downstream contraction was included in the final models since this was stabilizing to the computations and more representative of the experiment. Meshing of the CFD model was performed in the ANSYS Meshing module of Workbench. Two different refinements were generated by setting the maximum mesh size to 2 mm and 3 mm. In both cases, automatic inflation was used on the walls with a fixed first layer thickness of $1.64 \times 10^{-4}\text{ m}$. This near wall inflation was sufficient to cover the Reynolds number range and keep the y^+ value less than 300 for all conditions. Total element counts were 70 million elements for the fine grid and 20 million elements for the coarse grid. Some geometry to geometry differences in element count existed due to the various gap heights. The coarse mesh is designated “m0” below and the fine mesh “m1.” The coarse mesh is used unless designated as fine mesh results.

Computations were performed in ANSYS CFX. The unsteady Reynolds-averaged Navier-Stokes approach (URANS) approach was pursued using the Shear Stress Transport two-equation turbulence model. High resolution upwinding scheme was used for momentum, turbulence, and the scalar equation. Second-order backward Euler was used for the temporal discretization. For the scalar equation, since the variable was designed to vary between zero and unity, boundedness was enforced in the scalar transport equation through the additional variable definition. Limited time step sensitivity was performed. A fixed time step of 0.01 seconds was selected for all of the simulations. This made a volume turn over vary from 250 to 600 time steps for the cases of the balanced inlet Reynolds numbers of 100,000 and 40,000,

respectively. The RMS CFL (Courant-Friedrichs-Lewy) number was below 10 with a maximum CFL number in the domain of less than 100 for all cases. Simulations are performed for ten volume turn over times. Time averaging was performed over the last five volume turn over times.

Steady, fixed boundary conditions are applied to the simulations. At present, uniform inlet conditions are applied based on the Reynolds number. The inlet velocities are listed in Table 1. For turbulence inflow conditions, the medium intensity option is selected. To model the fluorescent dye used in the test apparatus, an Eulerian scalar field was used. Rather than attempting to model the dilute concentrations directly, a normalized difference was used, whose values ranged between zero and unity. The concentration is set to a value of one in Channel B and a value of zero in Channel A. For unbalanced flow conditions, the flow rate is varied in Channel A, as it was for the experiment. For balanced flow conditions, *i.e.* the same Reynolds number in both channels, a zero differential pressure is applied at the outlet boundaries. The downstream loop resistance was modified to match this condition for all balanced conditions as part of the test procedure.

For unbalanced conditions, two different outlet conditions are explored to examine the effect of back pressure on mixing. The differential pressure was only measured for the second phase of testing, *i.e.* in TS(b). In order to bound the influence of back pressure on mixing, the pressure difference from TS(b) is applied to TS(a). Because the gap is wider for TS(b) (9 inches) than TS(a) (2 inches), it is expected that the pressure difference for TS(b) will be higher and bounding, assuming the behavior is related to the width of the gap. The differential pressure was measured downstream of the gap and was recorded in inches of water. The data was reported for flow conditions and gap height, with a negative differential pressure recorded between Channel A and Channel B at the outlet, *i.e.* a lower pressure on the side of the lower flow rate. Rather than apply a negative relative static pressure at the outlet to Channel A, a positive relative static pressure was applied to the outlet of Channel B. Certain codes do not allow the specification of a negative static pressure difference, leading to this choice. Only 40×10^3 - 100×10^3 conditions are considered and the differential pressures for the gap geometry are presented in Table 2. For unbalanced flow, when the experimental pressure is applied, it is designated as “dpe;” when the pressure is equal at the outlets, the designation is “dp0.”

Table 1 Differential Pressure Applied to the Channel B Outlet for 40×10^3 - 100×10^3 Flow Conditions

Gap Height [mm]	Measured [in H ₂ O]	Back Pressure [Pa]
2	-8.09	2015
4	-3.30	822
6	-1.98	493
8	-1.51	376
10	-1.3	324
12 ¹	-1.25	311
14 ¹	-1.1	274
16 and above ¹	-1.0	249

¹ An estimate of the transition in gap height since the differential pressures are only reported at 10 and 20 mm. For gap heights ≥ 20 mm, the measured difference was -1.0 inch of water.

In order to compare to the mean mixing fractions computed, cross-sectional area-average monitors were set up at the inlets and exits to the model. The mass flow rates were monitored at all four openings. The concentration was monitored at the exit, with the value of 1 assumed at the Channel B inlet and 0 at the Channel A inlet. The monitor data was extracted from the results file and processed in MATLAB (v2013a, MathWorks, Natick, MA). The MATLAB program reads the CSV files, plots, and processes the

time series. In the time series, three initial volume turn over times are skipped. For each time series processed, a mean and the standard deviation is determined for each monitored quantity. The average values are then used to determine the interchange factors in the same manner as the processing of the experimental data. These results are stored into MATLAB structures analogous to the structures in which the experimental results are stored. This allows for re-use of the existing MATLAB code for co-plotting the computational and experimental results.

Additional post-processing is performed using FIELDVIEW (v. 14.0, Intelligent Light, Rutherford, NJ). At present, only visualizations are being performed. Both vortex core [21] and λ_2 vortex identification [22] methods have been applied to the transient flow field. An example is presented in figure 4, where the cut planes show the contour of the modeled tracer, the green lines are the vortex core method and the silver iso-surface the λ_2 -criteria. The vortex core method is applied by subtracting off the mean velocity field to highlight the local transient structures. Both methods highlight the structure of the translating vortices; however, the vortex core method more clearly demonstrates the angle of the vortices with respect to the gap and will be the favored method in the discussion on coherent structures below.

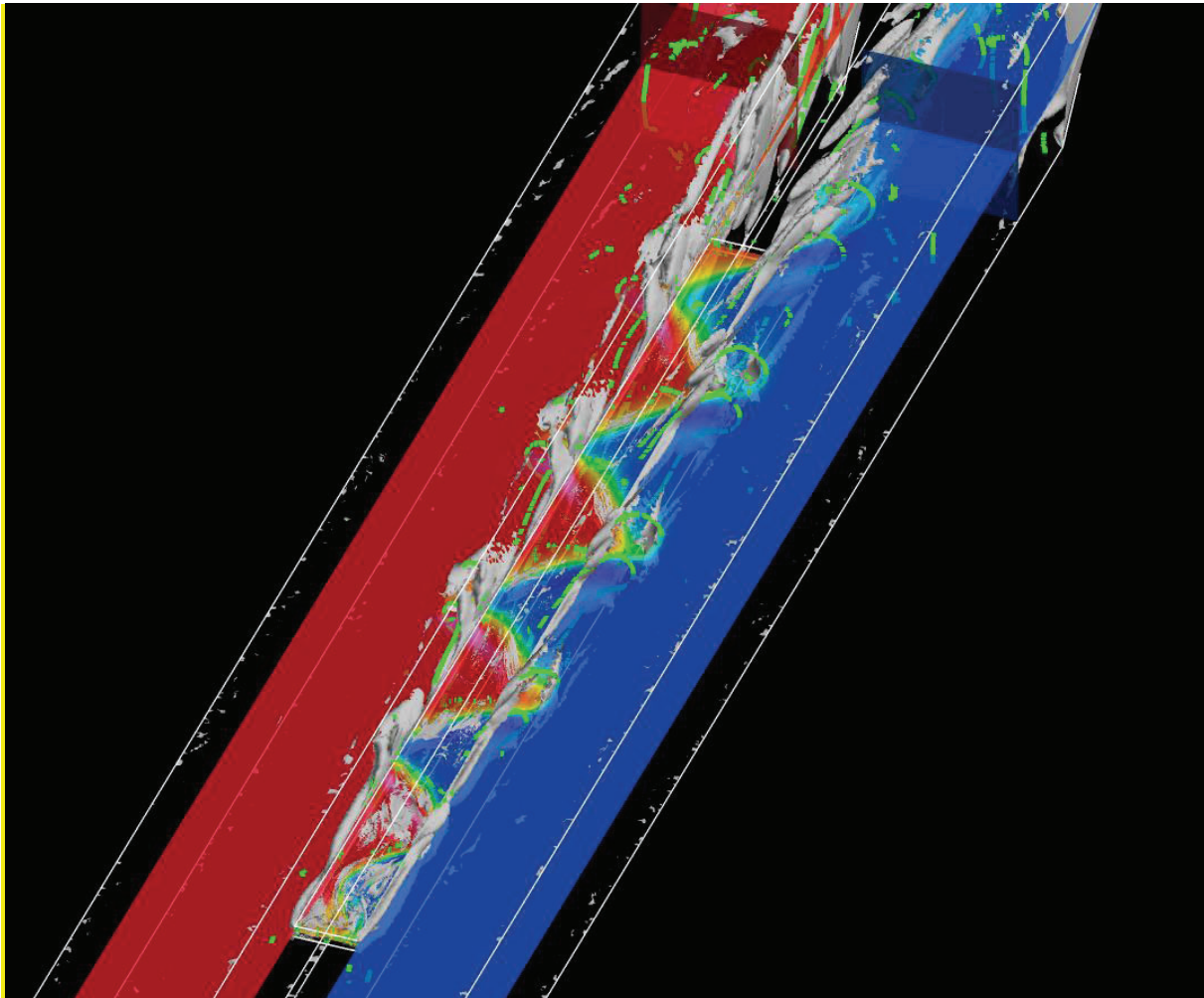


Figure 4. Snapshot of the CFD results for the 10mm gap with $Re = 100k$ & $100k$ inlet flow. The contour is of the tracer. The silver iso-surfaces are a λ_2 vortex visualization scheme, and the green lines are a vortex core identification scheme. The puffs nestle inside the vortices as expected.

3. INTEGRAL MIXING

To calculate the integral mixing coefficients through the gap based on the conservation of mass of the water and of the tracer, whose concentration is C in units of kg of tracer per kg of water, the test section can be divided into three control volumes as shown in figure 5.

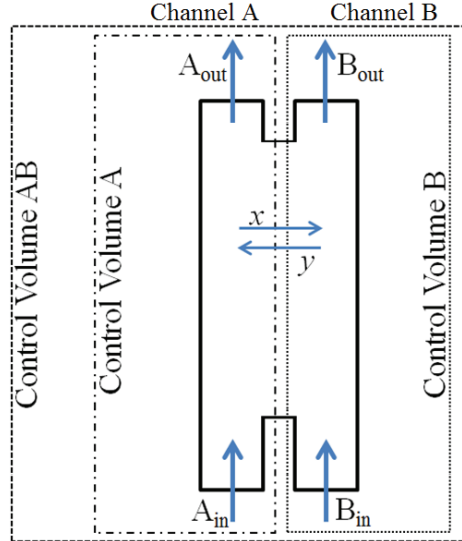


Figure 5. The test section and three control volumes considered.

From global control volume AB for the entire test section:

$$\dot{m}_{A,out} + \dot{m}_{B,out} = \dot{m}_{A,in} + \dot{m}_{B,in} \quad (1)$$

$$\dot{m}_{A,out} C_{A,out} + \dot{m}_{B,out} C_{B,out} = \dot{m}_{A,in} C_{A,in} + \dot{m}_{B,in} C_{B,in} \quad (2)$$

Where from control volumes around channels A and B in test section, as shown in figure 5, by definition

$$\dot{m}_{A,out} = \dot{m}_{A,in}(1 - x) + \dot{m}_{B,in}y \quad (3)$$

$$\dot{m}_{B,out} = \dot{m}_{A,in}x + \dot{m}_{B,in}(1 - y) \quad (4)$$

$$\dot{m}_{A,out} C_{A,out} = \dot{m}_{A,in} C_{A,in}(1 - x) + \dot{m}_{B,in} C_{B,in}y \quad (5)$$

$$\dot{m}_{B,out} C_{B,out} = \dot{m}_{A,in} C_{A,in}x + \dot{m}_{B,in} C_{B,in}(1 - y) \quad (6)$$

Here x is fraction transferred from A to B, and y is the fraction transferred from B to A. The simplest case is one where the flow speeds are equal and inlet concentration at one channel inlet is zero. *I.e.* we find solution to 5 & 6 assuming $x = y$, $\dot{m}_{A,out} = \dot{m}_{B,out} = \dot{m}_{A,in} = \dot{m}_{B,in}$ and $C_{A,in} = 0$ to get

$$x_5 = y_5 = \frac{C_{A,out}}{C_{B,out} + C_{A,out}} \quad (S5)$$

For cases where the flow speeds are not equal, we can easily derive four more solutions for both mixing coefficients. For example; solving equations 3 and 5 yields:

$$x_1 = 1 - \frac{\dot{m}_{A,out}(C_{A,out} - C_{B,in})}{\dot{m}_{A,in}(C_{A,in} - C_{B,in})} \quad \text{and} \quad y_1 = \frac{\dot{m}_{A,out}(C_{A,in} - C_{A,out})}{\dot{m}_{B,in}(C_{A,in} - C_{B,in})} \quad (S1)$$

Similarly we get x_2 and y_2 (S2) after solving equations 4 and 6, x_3 and y_3 (S3) after solving equations 3 and 6, and x_4 and y_4 (S4) after solving equations 4 and 5.

3.1 Balanced Flow Results

For balanced flow figures 6 and 7 show the comparison between experimental results and CFD predictions for the highest and lowest flow rates. We can see that the data agree well within the bounds of uncertainty for TS(a) data. However, for TS(b), the model fails to correctly predict the mixing. At present, there is not a clear reason for the under-prediction of the mixing in TS(b) for balanced conditions and is the subject of future work.

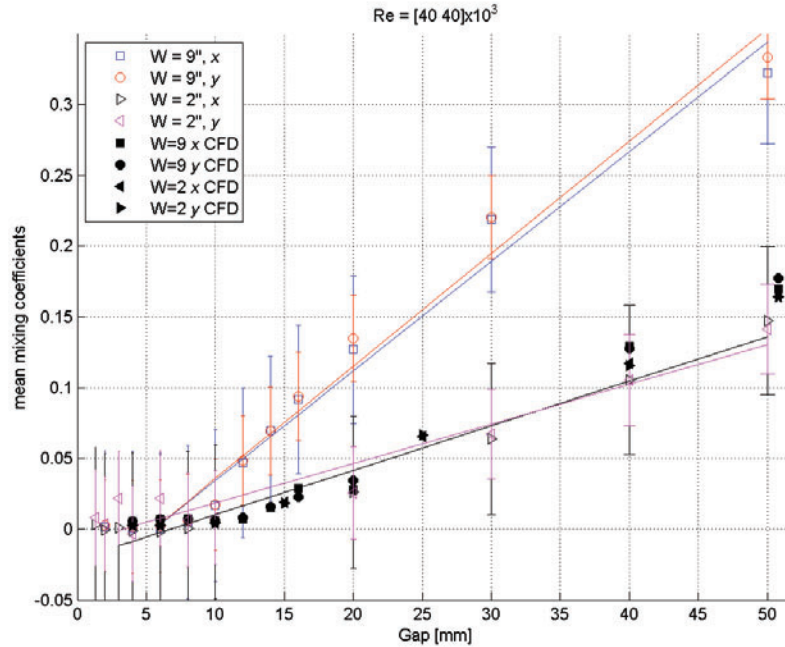


Figure 6. Comparison of TS(a) and TS(b) mixing coefficients for $Re = [40\ 40] \times 10^3$.

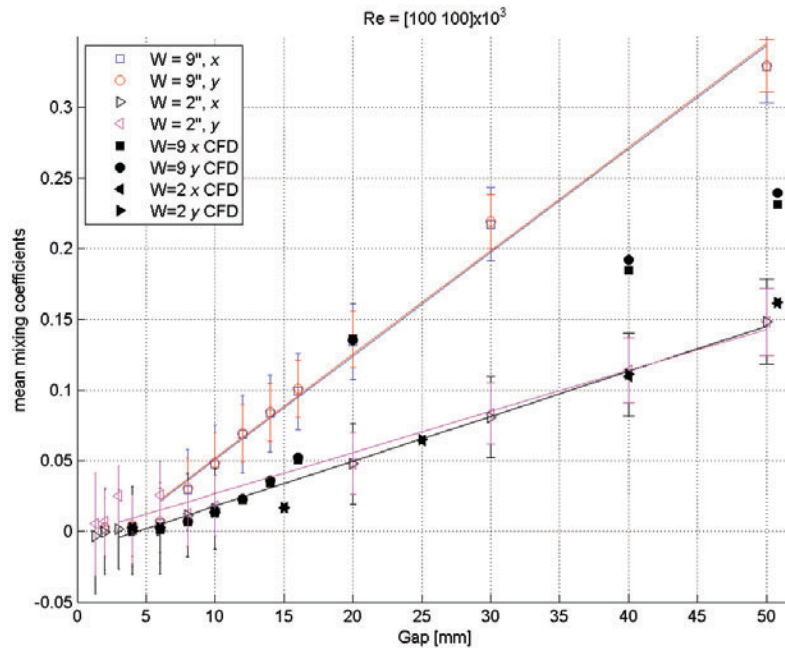


Figure 7. Comparison of TS(a) and TS(b) mixing coefficients for $Re = [100\ 100] \times 10^3$.

Over the tested range, the mixing rate as a function of gap height can be seen to be nominally independent of channel Reynolds number. The higher mixing coefficients found with the wider gap are assumed to be due to the relatively larger coherent structures discussed in Section 4. We can note that within the uncertainty of the measurement and as expected, for both test sections there was no significant net leakage ($x = y$), no significant mass transfer for gaps below 6 mm, mixing monotonically increased beyond an 8mm gap, and mixing appears to be independent of channel Re. We can also note that at the largest gap opening for TS(b) the mixing coefficient deviates from a linear trend, going from over to under the trend line indicating a decrease in mixing with increasing gap height. Presumably, the mixing approaches a maximum when the finite channel size limits the mixing reservoir.

3.2 Unbalanced Flow Results

For unbalanced flow there exists a pressure difference between channels A and B, and for the larger gap heights the mass flow rates in channels A and B had nominally balanced by the end of the test section. The mass transfer occurs predominantly from the high inlet speed channel B to the low speed channel A (*i.e.* $y > x$). If mixing was due to purely pressure driven one-way mass transfer from channel B to A and flow balanced perfectly by end of test section, then by definition the result would be

$$x = 0 \text{ and } y = \frac{1}{2} \left(1 - \frac{\dot{m}_{A,in}}{\dot{m}_{B,in}} \right), \quad (7)$$

which we call the one-way mixing limit. For $[Re_{Dh,A} \ Re_{Dh,B}] = [40 \ 100], [60 \ 100]$ and $[80 \ 100] \times 10^3$ this would lead to $y = 0.3, 0.2$ and 0.1 , respectively. In figures 8 through 10 the solid black line shows the expected value of coefficient y , if mixing were due to one-way mass transfer alone. The results from Eq. (7) is designated by “Theory” in the legends. We see that as the gap becomes larger and the unbalance in flow rates gets smaller, mixing due to the shear layer becomes more significant and the large coherent structures are more apparent.

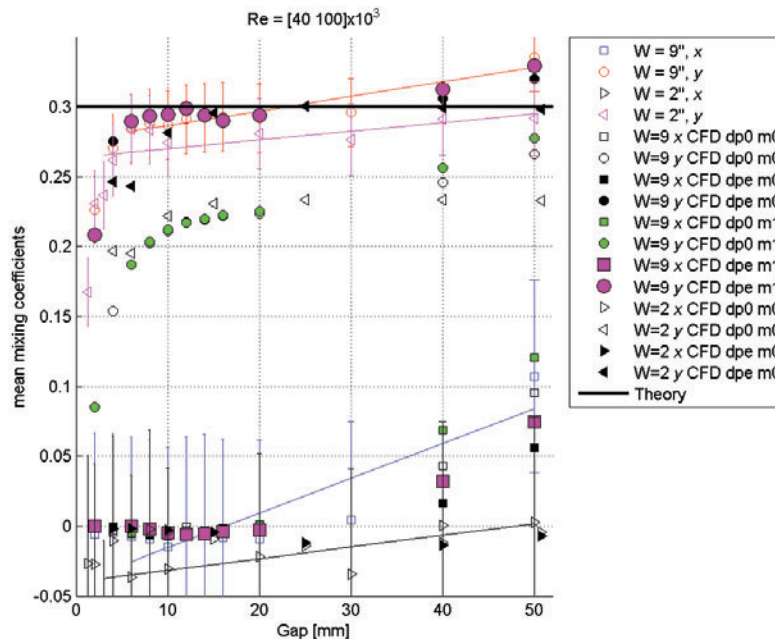


Figure 8. Comparison of TS(a) and TS(b) mixing coefficients for $Re = [40 \ 100] \times 10^3$

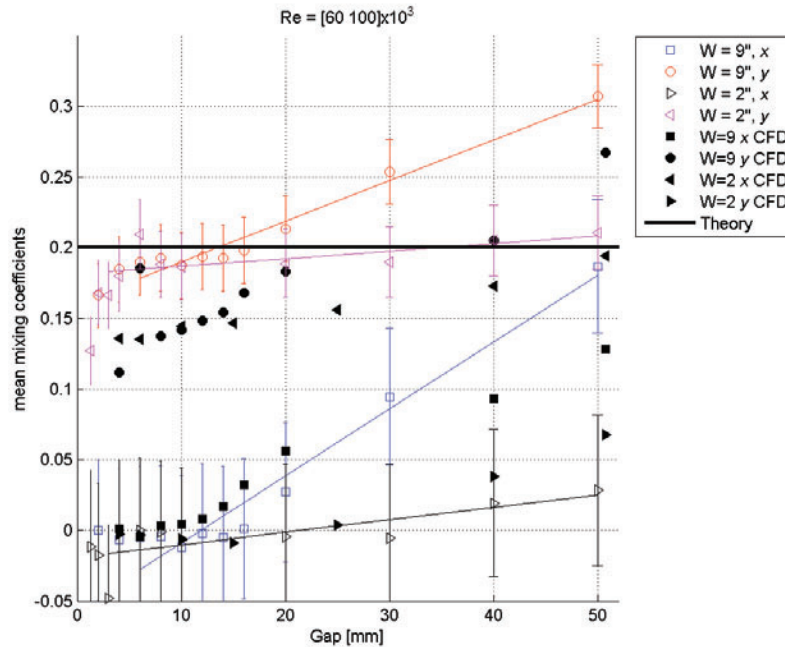


Figure 9. Comparison of TS(a) and TS(b) mixing coefficients for $Re = [60\ 100] \times 10^3$.

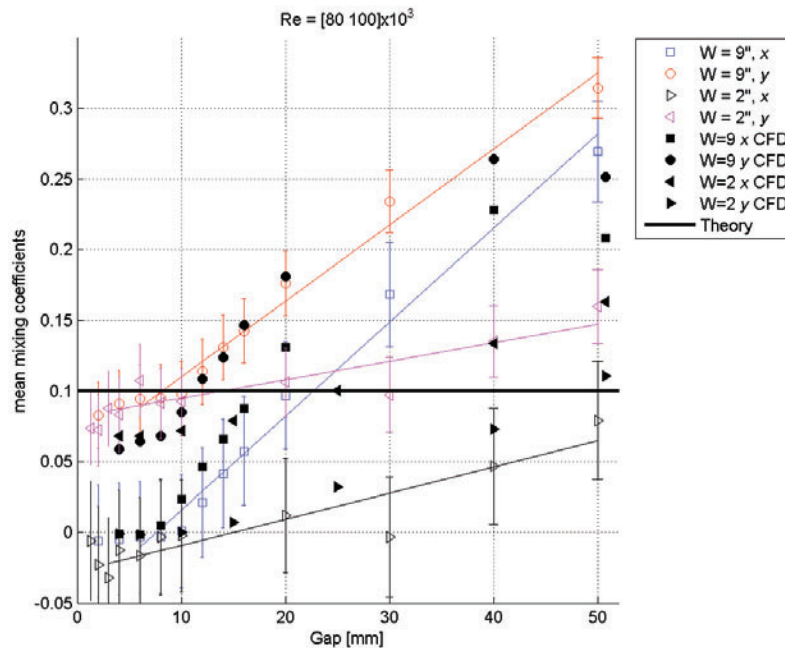


Figure 10. Comparison of TS(a) and TS(b) mixing coefficients for $Re = [80\ 100] \times 10^3$.

Figures 8 through 10 compare the mixing coefficients found experimentally and computationally for TS(a) and TS(b). We can observe that for large Reynolds number differences between the channels (ΔRe), the measured mass transfer approaches one way mixing limit for gaps larger than 4 mm and exceeds the one way limit in all cases for TS(b). As the gap becomes larger and ΔRe smaller, mixing due to the shear layer becomes more significant and the mixing is more than expected simply due to the

pressure difference balancing out the flows. The computational results under predict the mass transfer coefficient γ for the large $\Delta Re = (Re_{Dh,B} - Re_{Dh,A})$ cases when no pressure differential is applied at the outlet, but matches well as the ΔRe decreases. The discrepancy between experiment and numerical is due to the presumed versus actual outlet pressures. This is explored in more detail in figure 8. In figure 9 and 10, the computational results use boundary conditions at the outlet with pressures set to be equal. In figure 8, the role of back pressure variation and mesh refinement is explored in more detail. In this figure for the CFD results, m0 designates the coarse mesh and m1 the fine mesh; dp0 the zero difference in pressure between the outlets and dpe the experimental difference in pressure. For the most part, grid resolution does not play a large factor, with significant differences only notable at the largest gap heights. The largest single contributor is the applied back pressure. When the experimental pressure difference is applied, the computational mixing coefficients match the observations. Worth noting, for large gap heights, when the pressure difference is applied, the mass flow rates for each channel equilibrate to a consistent value. Without the back pressure applied, the mass flow rate at the outlet for channel A is less than that for channel B which helps explain the under prediction of mixing based on Eq. (S1). This suggests that for larger gap heights, a better boundary condition for the CFD would be an equal flow split as an approximation.

4. ON THE COHERENT STRUCTURES

For balanced inlet flow rates, the bulk of the mixing was expected to be due to the large scale structures that arise from a Kelvin-Helmholtz type instability, as discussed by Meyer [9]. The large structures carry the fluid across the gap and lead to the “puffs” of dye observed as the large structures exit the gap. In figure 11a we see a typical instantaneous velocity field showing the large scale structures, conceptual sketch of the flow in a gap and a photo from the current experiments. The periodic “puff” of tracer dye seen in the photo in figure 12 shows the mixing due to the coherent structures from two views taken simultaneously at 90° with respect to each other in both TS(a) and TS(b).

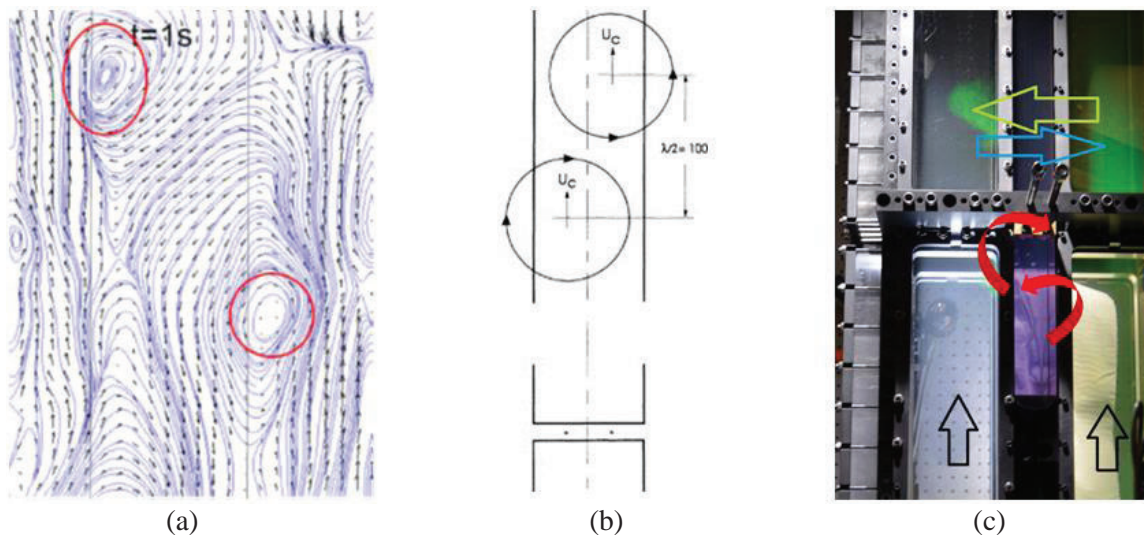


Figure 11. a) Vortex street in a narrow gap visualized via PIV by Lexmond *et al.* [20]. This is a typical instantaneous velocity field showing the large scale structures, and similar to what we observed via PIV reported in [25, 26]. (b) Flow model for the gap region by Meyer and Rehme [1]. (c) photo with a periodic ‘puff’ in TS(a). Similar, albeit larger, puffs were observed in TS(b).

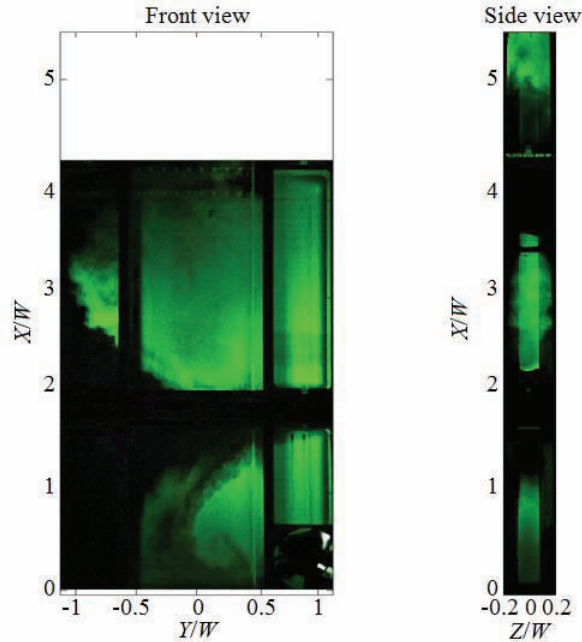


Figure 12. The coherent flow structures at $Re = 100,000$ made visible by dye injection to the right side channel upstream of the gap. The gap begins at $X/W = 0$. Channels span $Y/W = \pm(0.5 \text{ to } 1.1)$. The dimensions are normalized by the gap width $W = 229$ mm. Flow is from bottom up.

From the temporal frequency of the puffs (*i.e.* frequency of the coherent structures), f , we can define the Strouhal number, as $St = fW/U$. For TS(a) with St defined based on the convection speed of the average Strouhal number was found to be 0.22 and 0.23 for the 20 and 50 mm gap heights, respectively. For TS(b) with St defined based on the average flow speed of the average Strouhal number was found to be 0.24 and 0.25 for the 20 and 50 mm gap heights, respectively. While they did not explicitly discuss it, the Strouhal number of Lexmond [20] is 0.21, as they had a 21 mm wide gap, flow speed of 11.1 cm/s and frequency of 1.1 Hz.

4.1 Coherent Structures as Shown by PIV and CFD

Figure 13 shows some of the key flow structures found in the side channels *via* Tomographic PIV as a “puff” is exiting the gap. In figure 14 we can observe qualitatively similar vortex structures predicted by the CFD results, and the green “strings” are vortex cores identified using the method of Haimes [21] on a local velocity in time with the mean, time-averaged velocity subtracted. This is a Lagrangian frame of reference with respect to the flow. Each puff has a pair of counter-rotating hairpin-like vortices. The first draws fluid from the gap and the second terminates flow from the gap. The puffs in TS(a) grow quickly and then maintain the same size as they advect downstream. The puffs in TS(b) grow continuously once they appear and the puff dynamics relate to the tails on the hairpin vortices. In TS(a), the hairpins align with the gap for the first 20% of the gap length and then rotate such that they are perpendicular to the gap whereas in TS(b), the hairpins remain aligned with the gap for the entire length, and thus able to draw fluid from the gap for a much longer distance. This alignment of the vortices with the gap helps explain why TS(b) has higher mixing than TS(a). Future work will look to compare quantitatively the coherent structure size in the CFD to the tomographic PIV to determine the role of different length scales on the mixing coefficient. In particular, for the model of TS(b), the large scale structures are represented, but the mixing is under predicted. This suggests that the smaller length scales may also play a role in determining the exchange through the gap.

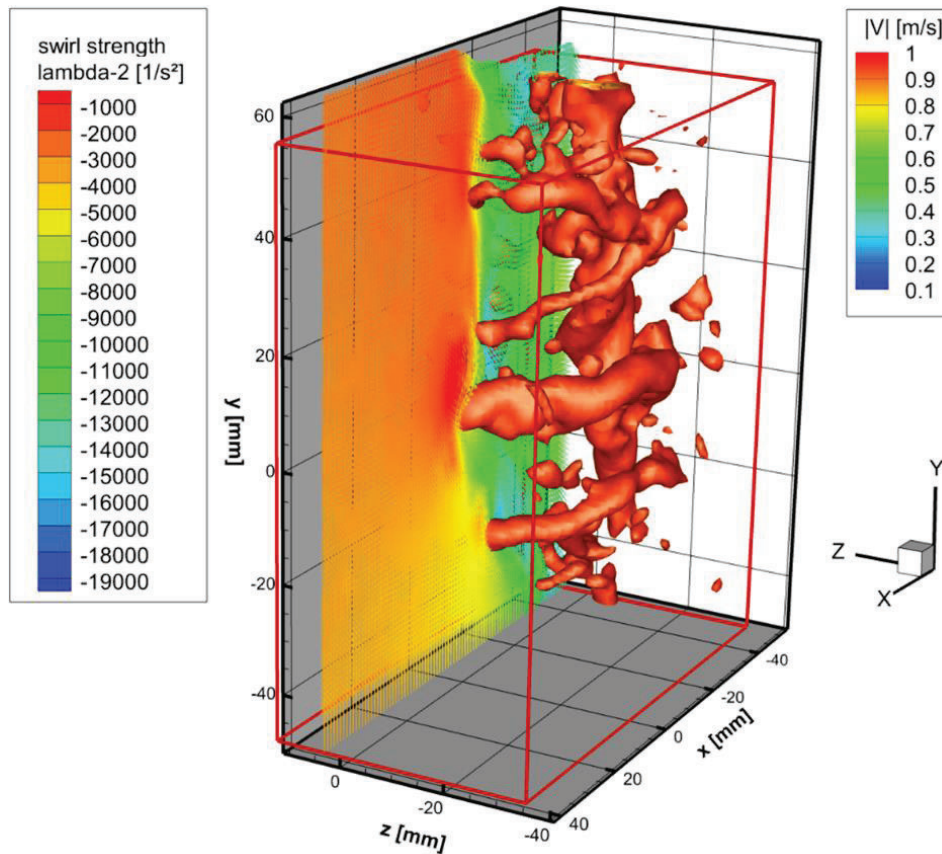


Figure 13. Sample on Tomographic PIV data showing a puff exit a 20 mm gap at $Re = 100,000$ in both channels. In this figure the gap's center is at $z = 0$ and edge at $x = -40$ mm.

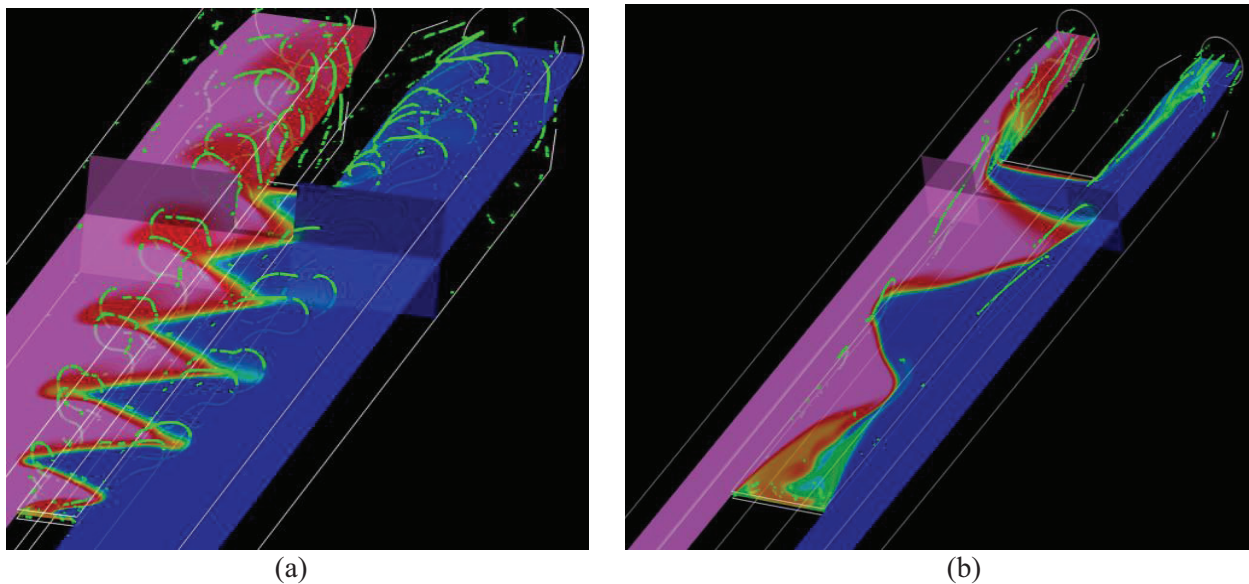


Figure 14. Visualization of CFD results of mixing (a) in TS(a) and (b) in TS(b). The contour map is normalized to span from zero concentration (blue) to one (magenta). The green "strings" are vortex cores identified using the method of Haines [21].

5. CONCLUSIONS

For this project, a new flow loop with two test sections was designed and built. After verifying that the inflow was well conditioned, the integral mixing through various gap openings was measured. For balanced flow cases, there was no significant leakage below a gap height of 8 mm. With larger gap heights, the coherent structures reported by previous investigators were observed, and the mixing trends appeared to be independent of the channel Re_{Dh} for the range investigated. With wider gap of TS(b), the structures were larger and caused relatively more mixing than in TS(a), as the side channel dimensions remained unchanged. For the unbalanced flow cases with large ΔRe , the measured mass transfer approached the one-way mixing limit. Mixing due to the coherent structures became more significant with increasing gap height and decreasing ΔRe . For TS(a), data the measured bulk mixing trends compared well with CFD predictions, with some differences in the initial CFD results due to a simplified zero differential pressure assumption at the outlet. PIV measurements and high-speed videos were utilized to further examine the dynamics of the flow and the dimensionless frequency of the coherent structures was in satisfactory agreement with observations by previous investigators. The analysis of the results, higher fidelity CFD, and more detailed comparison between the experimental and CFD data is ongoing.

NOMENCLATURE

BL	Boundary layer
C	Concentration (kg/kg)
D_h	Hydraulic diameter, 0.127 m
H_s	Shape factor
LDV	Laser Doppler Velocimetry
\dot{m}	Mass flow rate (kg/s)
Re_{Dh}	Reynolds number based on the hydraulic diameter of the channel
PIV	Particle image Velocimetry
ppb	Parts per billion (kg/kg)
St	Strouhal Number
TS(a)	Test section (a)
TS(b)	Test section (b)
x	Mixing coefficient, fraction of incoming flow from channel A transferred to channel B
y	Mixing coefficient, fraction of incoming flow from channel B transferred to channel A
X, Y, Z	Streamwise, normal to gap width and along gap width coordinates (m)
W, L, H	Gap width, length and height (m)

REFERENCES

1. Meyer, L., and Rehme, K., "Large-Scale Turbulence Phenomena in Compound Rectangular Channels", *Experimental Thermal and Fluid Science*, **8**, pp. 286-304 (1994).
2. Mahmood, A., Rohde, M., van der Hagen, T.H.J.J., and Mudde, R.F., "Contribution of Large-Scale Coherent Structures towards the Cross Flow in Two Interconnected Channels", *13th International Topical Meeting in Nuclear Reactor Thermal Hydraulics*, Kanazawa City, Japan, Sept. 27th – Oct. 2nd, (2009).
3. F. Baratto, S.C.C. Bailey and S. Tavoularis, "Measurements of frequencies and spatial correlations of coherent structures in rod bundle flows", *Nucl. Eng. Des.*, **236**, pp. 1830–1837 (2006).
4. W. Eifler and R. Nijssing, "Experimental investigation of velocity distribution and flow resistance in a triangular array of parallel rods", *Nucl. Eng. Des.*, **5**, pp. 22–42 (1967).
5. T. Krauss and L. Meyer, "Characteristics of turbulent velocity and temperature in a wall channel of a heated rod bundle", *Exp. Thermal Fluid Sci.*, **12**, pp. 75–86 (1996).

6. T. Krauss and L. Meyer, "Experimental investigation of turbulent transport of momentum and energy in a heated rod bundle", *Nucl. Eng. Des.*, **180**, pp. 185–206 (1998).
7. S.V. Möller, "On phenomena of turbulent flow through rod bundles", *Exp. Thermal Fluid Sci.*, **4**, pp. 25–3 (1991).
8. S.V. Möller, "Single-phase turbulent mixing in rod bundles", *Exp. Thermal Fluid Sci.*, **5**, pp. 26–33 (1992).
9. Meyer, L. "From discovery to recognition of periodic large scale vortices in rod bundles as source of natural mixing between channels - A review" *Nuclear Engineering and Design*, 1575–1588 (2010).
10. D. Chang and S. Tavoularis, "Convective heat transfer in turbulent flow near a gap", *J. Heat Transfer* **128**, pp. 701–708 (2006).
11. D. Chang and S. Tavoularis, "Numerical simulation of turbulent flow in a 37-rod bundle", *Nucl. Eng. Des.* **237**, pp. 575–590 (2007).
12. D. Home, G. Arvanitis, M.F. Lightstone and M.S. Hamed, "Simulation of flow pulsations in a twin rectangular sub-channel geometry using unsteady Reynolds Averaged Navier–Stokes model", *Nucl. Eng. Des.* **239**, pp. 2964–2980 (2009).
13. Derksen, J.J., "Simulations of lateral mixing in cross-channel flow" *Computers & Fluids*, **39**, Issue 6, pp.1058-1069 (2010).
14. Home, D., and Lightstone, M. F. "Numerical investigation of quasi-periodic flow and vortex structure in a twin rectangular subchannel geometry using detached eddy simulation." *Nuclear Engineering and Design*, **270**, pp. 1–20 (2014)
15. Merzari, E., Ninokata, H., Mahmood, A., and Rohde, M., "Proper orthogonal decomposition of the flow in geometries containing a narrow gap", *Theor. Comput. Fluid Dyn.*, **23**, pp. 333–351 (2009).
16. Jordan Ko, Didier Lucor, and Pierre Sagaut "Sensitivity of two-dimensional spatially developing mixing layers with respect to uncertain inflow conditions" *Phys. Fluids*, **20**, 077102 (2008).
17. Anselmet, F., Ternat, F., Amielh, M., Boiron, O., Boyer, P., and Pietri, L., "Axial development of the mean flow in the entrance region of turbulent pipe and duct flows", *C. R. Mecanique*, **337**, pp. 573–584 (2009).
18. Clauser, F.H. "Turbulent boundary layers in adverse pressure gradients," *J. Aeronaut. Sci.*, **21**, pp. 91–108 (1954).
19. Tropea, C., Yarin, A.L., and Foss, J.F. *Springer Handbook of Experimental Fluid Mechanics*, 2007.
20. Lexmond, A.S., Mudde, R.F., and van der Hagen, T, "Visualization of the Vortex Street and Characterization of the Cross Flow in a Gap Between Two Sub-Channels", *NURETH-11*, Avignon, France (2005).
21. R. Haimes and D. Sujudi, "Identification of Swirling Flow in 3D Vector Fields," *Technical Report, Department of Aeronautics and Astronautics*, MIT, Cambridge, MA (1995).
22. J. Jeong and F. Hussain, "On the Identification of a Vortex," *Journal of Fluid Mechanics*, Vol. 285, pp. 69-94 (1995).